

Electric-field-controllable high-spin SrRuO₃ driven by a solid ionic junction

Jingdi Lu^{1#}, Liang Si^{2, 3#}, Xiefei Yao^{1#}, Chengfeng Tian^{1#}, Jing Wang^{4#}, Qinghua Zhang^{5#}, Zhengxun Lai⁶, Iftikhar Ahmed Malik¹, Xin Liu¹, Peiheng Jiang², Kejia Zhu⁵, Youguo Shi⁵, Zhenlin Luo⁷, Lin Gu⁵, Karsten Held³, Wenbo Mi⁶, Zhicheng Zhong^{2*}, Ce-Wen Nan⁴ and Jinxing Zhang^{1*}

1. Department of Physics, Beijing Normal University, 100875 Beijing, China
2. Key Laboratory of Magnetic Materials and Devices, Ningbo Institute of Materials Technology and Engineering, Chinese Academy of Sciences, Ningbo, 315201 China
3. Institut für Festkörperphysik, TU Wien, Wiedner Hauptstraße 8-10, 1040 Vienna, Austria
4. School of Materials Science and Engineering, Tsinghua University, 100084 Beijing, China
5. Institute of Physics, Chinese Academy of Science, 100190 Beijing, China
6. Tianjin Key Laboratory of Low Dimensional Materials Physics and Preparation Technology, School of Science, Tianjin University, Tianjin 300354, China
7. National Synchrotron Radiation Laboratory & CAS Key Laboratory of Materials for Energy Conversion, and Department of Physics, University of Science and Technology of China, Hefei 230026, China

#These authors contributed equally to this work.

*E-mail: zhong@nimte.ac.cn; jxzhang@bnu.edu.cn

Controlling magnetism and spin structures in strongly correlated systems by using electric field is of fundamental importance but challenging. Here, a high-spin ruthenate phase is achieved via a solid ionic chemical junction at $\text{SrRuO}_3/\text{SrTiO}_3$ interface with distinct formation energies and diffusion barriers of oxygen vacancies, analogue to electronic band alignment in semiconductor heterojunction. Oxygen vacancies trapped within this interfacial SrRuO_3 reconstruct Ru-4d electronic structure and orbital occupancy, leading to an enhanced magnetic moment. Furthermore, an interfacial magnetic phase can be switched reversibly by electric-field-rectifying oxygen migration in a solid-state ionic gating device, providing a framework for atomic design of functionalities in strongly correlated oxides using a way of solid chemistry.

Controlling magnetism and low-dimensional spin textures in strongly correlated systems by electric field is fundamentally significance due to their potential applications in information processing with low-power consumption [1-4]. Over past decades, spin degree of freedom have been effectively controlled by electric field in magnetoelectrics and multiferroic heterostructures [5-11]. However, a combination and control of these ferroic orderings with advanced characterizations of those coupled behaviors is still fundamentally challenging [1,3]. Therefore, it is desirable to design new correlated electron systems with an atomic precision by engineering of material chemistries and architectures [3]. Transition metal oxides (TMOs) with strong *d*-electron correlations and spin-orbit coupling (SOC) may provide an effective platform towards emergent magnetism with controllable spin textures [12-20].

SrRuO₃ (SRO) is a unique 4*d* TMO with a coexistence of SOC and itinerant ferromagnetism [21], leading to a large variety of physical behaviors which have been experimentally observed such as high-spin states driven by crystal orientations [22-24], magnetic skyrmions due to the broken symmetry [25-28], and metal-insulator transition [29-31], etc. More importantly, emergent physical behaviors have been theoretically proposed in SRO recently [13,15,32,33], triggering a broad attention to discover the potential quantum states in this material. Among these theories, heavy electron doping in SRO seems to be effective to further enhance magnetism and change electronic structure [15], which is, however, experimentally challenging in this oxide with a metallic ground state. Although a high concentration of the oxygen vacancy (V_o) is

equivalent to electron doping, it is hard to be achieved in bulk SRO. This gives a strong impetus to explore an alternative pathway to build upon the above physical scenario. Inspired by electrons rectifying at solid-state junctions, such as the well-known diode at p - n junctions [34], a solid ionic chemical junction may be used to rectify V_o by using its chemical discontinuity across the interface [35].

Atomically flat SRO thin films with accurate thicknesses of 5 uc, 10 uc, 30 uc and 50 uc (where uc is unit-cell) were grown on (001)-oriented SrTiO₃ (STO) substrates with TiO₂-termination by pulsed laser deposition (PLD) with *in-situ* reflection high-energy electron diffraction (RHEED). Through a synchrotron-based X-ray diffraction (SXRD) study, a set of (002)-oriented peaks in Fig. 1 (a) reveal SRO thin films with a c -axis lattice constant of 3.967 Å (thickness up to 50 uc). The epitaxial growth of SRO thin films is shown in Fig. S1. High-resolution scanning transmission electron microscopy (STEM) in Fig. 1 (b) indicates a high-quality and dislocation-free epitaxy for the SRO thin films. The out-of-plane and in-plane lattice structures in STEM (Fig. 1 (c)) illustrates that there is an in-plane compressive strain (~ -0.45 %) without any relaxation and phase separation across the whole SRO thin films, which are consistent with the results obtained from the x-ray reciprocal space mapping (RSM) (Fig. 1 (d)). The monoclinic structure of the SRO thin films [36] have been further revealed by the x-ray RSM. The details of growth and measurements can be seen in supplementary methods.

The ferromagnetic Curie temperature (T_C) was measured as a function of thickness by temperature-dependent magnetization and resistivity (M - T and R - T) [21,37]. As shown in the Fig. 2 (a) and (b), $T_C \sim 153$ K is observed for the 5 uc SRO thin film, while another $T_C \sim 125$ K appears with the thickness increasing from 10 uc to 50 uc, the decreased T_C is ascribed to the fully strained monoclinic structure as studied previously [36,38]. The thickness-dependent magnetic hysteresis loops along the pseudo [001] axis were measured by superconducting quantum interference device (SQUID) (Fig. 2 (c)). Upon increasing the thickness from 5 uc to 10 uc, a step-like hysteresis with two coercive fields appears, which are more obvious in the 30 uc and 50 uc thin films. For the 5 uc SRO, the out-of-plane saturated moment (M_s) is $\sim 2.18 \mu_B/\text{formula unit (f. u.)}$, which is higher than the one of low-spin state of SRO ($\sim 1.1 - 2.0 \mu_B/\text{f. u.}$ in experiments and theories, $2.0 \mu_B/\text{f. u.}$ from full Hund's rule) [39-42]. As the thickness increases, the M_s decreases to ~ 2.06 , ~ 1.75 and $\sim 1.28 \mu_B/\text{f. u.}$ for 10, 30, and 50 uc SRO, respectively, indicating that the SRO at the interface contributes to the enhancement of M_s as shown in insets of Fig. 2 (c) and (d). The magnetic domain switching, corresponding to the hysteresis, has been characterized by using low-temperature magnetic force microscopy (MFM) at 10 K. For the 5 uc SRO, a mono-domain switching occurs (Fig. S2). However, for the SRO thin film with a thickness above 10 uc, there is a distinctive switching with two coercive fields at low/high magnetic field (Fig. S3), which further indicates that the step-like magnetic hysteresis could be attributed to a separation of magnetic phases: interfacial-SRO (high T_C/moment) and top-SRO (low T_C/moment). The hysteresis behavior as a function of top-SRO thickness is simulated in Fig. S4, which is consistent

to our experimental observations in Fig. 2 (c). The details of measurements for magnetic/electrical characterizations are given in supplementary methods and Fig. S5.

In these fully-strained SRO thin films without lattice relaxation, slight alternation of chemical structure at the interface may play a key role on the enhanced magnetization [43]. As seen from bright-field STEM in Fig. 3 (a) and (b), the interfacial-SRO phase presents more V_o which is negligible in the top-SRO. Depth-profiling X-ray photoelectron spectroscopy (XPS) with *in-situ* etching of surface layers without damaging underlying layers (see Fig. 3 (c) for the schematics) shows the valence states of Ru at various etching depths for the 50 uc SRO in Fig. 3 (d). The binding energy of Ru $3d_{3/2}$ remains at ~ 282.82 eV while etching away up to 30 uc. However, it starts to dramatically decrease by ~ 1.3 eV when the etching depth reaches about 45 uc, indicating that Ru^{3+} appears at the interfacial-SRO [44]. At all conditions, there are no change for the binding energies of Sr $3d$ from the top-SRO to interfacial-SRO and then STO (see Fig. S6). Therefore, the appearance of Ru^{3+} at the interfacial-SRO is induced by the V_o based on the above analysis of STEM and XPS results [44]. The details of measurements for chemical characterizations are given in supplementary methods.

The microscopic origin of this V_o -dominant interfacial-SRO phase with enhanced M_s can be understood by calculating formation energy (E_{OF}) and diffusion barrier (E_b) of the V_o in both SRO and STO. The E_{OF} is defined as

$$E_{OF} = E_{SC}(V_o) - E_{SC} + E(O_2)/2,$$

for both SRO and STO in density functional theory (DFT). Here, $E_{SC}(V_o)$ and E_{SC} are the energies of supercells with and without a V_o , respectively, and $E(O_2)$ is the energy of a single O_2 molecule. The E_{OF} of bulk SRO is ~ 4.7 eV, which is ~ 2 eV lower than that of bulk STO, indicating that the V_o prefers to be on the SRO side. Near the SRO/STO interface, the E_{OF} of a single V_o in SRO is ~ 4 eV, lower than that in STO (Fig. 3 (e)). Therefore, we expect that V_o migrates into the interfacial-SRO phase when SRO is in contact with STO. In the Fig. S7, we further calculated the diffusion energy barrier E_b of V_o . In SRO, E_b is ~ 1.4 eV, which is much higher than the one in STO (~ 0.6 eV). While for STO, such a barrier height permits V_o diffusion and in SRO it prevents V_o diffusing further into the SRO film [45]. As a result, the V_o is trapped at the interfacial-SRO phase as visualized in Fig. 3 (e), and forms a V_o diode, in a similar way as electron diffusion in a conventional electrical diode.

For understanding the role of V_o in the enhanced M_s at the interfacial-SRO phase, we construct a SRO (5 uc)/STO (4 uc) heterostructure, where one oxygen atom is removed between the 2nd and 3rd RuO_2 layers to model the V_o (see Fig. 4 (a) and (b)). There is a substantial spin and orbital reconstruction of the Ru d -electrons near the V_o . The occupation of Ru d_{z^2} -orbit arises from the fact that i) V_o provides abundant electrons, and ii) it breaks the neighboring RuO_6 octahedron and changes the crystal-field splitting. The latter shifts the energy of d_{z^2} -orbit down by forming bonding and

anti-bonding states. This orbital reconstruction is pivotal for turning the $4d^4$ low-spin state ($S = 1$, $\sim 1.5 \mu_B/\text{Ru}$, far away from V_o) into $4d^5$ high-spin state ($S = 3/2$, $\sim 2.3 \mu_B/\text{Ru}$, neighboring V_o) as shown in Fig. 4 (c) and (d), being compatible with our experimental results (Fig. 2 (d)). Thus, the interfacial-SRO phase with high spin can be defined as V_o -SRO phase. The computational details are attached in the supplementary materials.

The interfacial high-spin SRO phase originates predominately from the V_o contributions, which could be naturally controllable in this V_o diode across the solid V_o -SRO/STO chemical junction by an electric field [46]. The temperature-dependent transport measurements with *in-situ* magnetic-domain characterizations were performed in the 10 uc SRO thin film under the application of electric field as schematically shown in Fig. 5 (a). The details on measurements can be seen in supplementary methods. A reversible control of the V_o -SRO (T_C is ~ 153 K) was achieved by electric-field-driven uni-directional V_o migration from SRO to STO as shown in Fig. 5 (b), demonstrating that the V_o -SRO with high spin can be erased and rebuilt by applying electric field. With a magnetic bias between the coercive fields of V_o -SRO and top-SRO, the soft V_o -SRO will switch firstly and serve as an effective magnetic field (H_{eff}). Magnetic domain switching with and without the application of electric field has been performed under a magnetic bias of $+0.75$ T, which is lower than the coercive field of top-SRO in the 10 uc film (~ 1 T, see Fig. 2 (c)). With the application of the electric field of $+4 \text{ kV}\cdot\text{cm}^{-1}$, magnetic domains cannot be switched at the same magnetic bias as the V_o -SRO (namely H_{eff}) has been erased as shown in Fig.

5 (c).

In summary, by designing an oxygen ionic chemical junction, V_o are trapped at the interfacial-SRO phase, leading to an electronic and orbital reconstruction. As a result, a high-spin state at the V_o -SRO phase is achieved, which is reversibly switchable by an electric-field-induced oxygen migration in a solid-state ionic gating device. Furthermore, understanding of electronic and spin states in such a low-dimensional SRO phase makes this strongly correlated system a promising candidate for the further exploration and manipulation of emergent magnetism and spin structures.

Acknowledgements

We gratefully acknowledge the discussions with Prof. Nicola A. Spaldin in Materials Theory of ETH Zürich and Dr. L. Wang in Center for Correlated Electron Systems of Institute for Basic Science. The work is supported by the National Key Research and Development Program of China through Contract 2016YFA0302300 and 2016YFA0300102 and 2017YFA0303602, the Basic Science Center Program of NSFC under Grant No. 51788104, the National Natural Science Foundation of China (Grant No. 11974052, 11675179, 11774360, 11904373), and Beijing Natural Science Foundation (Z190008) and the CAS Interdisciplinary Innovation Team. L. Si and K. Held were supported by the European Research Council (ERC) under the European Union's Seventh Framework Program (FP/2007-2013) through ERC Grant No. 306447, and by the Austrian Science Fund (FWF) through project P 30997. Beamtime from APS 33BM and SSRF 14B and 3315 Program of Ningbo are appreciated.

Author contributions

J. Z. and Z. Z conceived the experiments and prepared the manuscript. X. Y. and C. T. fabricated the thin films. K.Z. and Y. S. prepared the SRO ceramic target. X. Y., Z. Lai, J. L., X. L. and C. T. performed the synchrotron x-ray diffraction, electrical transport and XPS measurements. X. Y. and J. W. carried out the SQUID measurement. L. S., P. J., Z. Z. and K. H. performed the theoretical calculations. I. M. and J. L. carried out the AFM and MFM measurements. Q. Z. and L. G. performed STEM measurement. Z. Luo performed the RSM measurement. J.Z., C.-W. N., Z. Z. and W. M. were involved in

the discussion and revision of the manuscript. All authors were involved in the analysis of the experimental and theoretical results.

Reference

- [1] F. Matsukura, Y. Tokura & H. Ohno. Control of magnetism by electric fields. *Nat. Nanotechnol.* **10**, 209 (2015).
- [2] S. Dong, J.-M. Liu, S.-W. Cheong & Z. Ren. Multiferroic materials and magnetoelectric physics: symmetry, entanglement, excitation, and topology. *Adv. Phys.* **64**, 519 (2015).
- [3] N. A. Spaldin & R. Ramesh. Advances in magnetoelectric multiferroics. *Nat. Mater.* **18**, 203 (2019).
- [4] N. A. Spaldin. Multiferroics beyond electric-field control of magnetism. *Proc. Math. Phys. Eng. Sci.* **476**, 20190542 (2020).
- [5] V. Garcia, M. Bibes, L. Bocher, S. Valencia, F. Kronast, A. Crassous, X. Moya, S. Enouz-Vedrenne, A. Gloter, D. Imhoff, C. Deranlot, N. D. Mathur, S. Fusil, K. Bouzehouane & A. Barthélémy. Ferroelectric control of spin polarization. *Science* **327**, 1106 (2010).
- [6] J. T. Heron, M. Trassin, K. Ashraf, M. Gajek, Q. He, S. Y. Yang, D. E. Nikonov, Y. H. Chu, S. Salahuddin & R. Ramesh. Electric-field-induced magnetization reversal in a ferromagnet-multiferroic heterostructure. *Phys. Rev. Lett.* **107**, 217202 (2011).
- [7] T. H. Lahtinen, J. O. Tuomi & S. van Dijken. Pattern transfer and electric-field-induced magnetic domain formation in multiferroic heterostructures. *Adv. Mater.* **23**, 3187 (2011).
- [8] P. J. Ryan, J. W. Kim, T. Birol, P. Thompson, J. H. Lee, X. Ke, P. S. Normile, E.

- Karapetrova, P. Schiffer, S. D. Brown, C. J. Fennie & D. G. Schlom. Reversible control of magnetic interactions by electric field in a single-phase material. *Nat. Commun.* **4**, 1334 (2013).
- [9] L. T. Chang, C. Y. Wang, J. Tang, T. Nie, W. Jiang, C. P. Chu, S. Arafin, L. He, M. Afsal, L. J. Chen & K. L. Wang. Electric-field control of ferromagnetism in Mn-doped ZnO nanowires. *Nano Lett.* **14**, 1823 (2014).
- [10] Y. S. Oh, S. Artyukhin, J. J. Yang, V. Zapf, J. W. Kim, D. Vanderbilt & S. W. Cheong. Non-hysteretic colossal magnetoelectricity in a collinear antiferromagnet. *Nat. Commun.* **5**, 3201 (2014).
- [11] K. J. A. Franke, B. Van de Wiele, Y. Shirahata, S. J. Hämäläinen, T. Taniyama & S. van Dijken. Reversible electric-field-driven magnetic domain-wall motion. *Phys. Rev. X* **5**, 011010 (2015).
- [12] M. Ziese, I. Vrejoiu, E. Pippel, P. Esquinazi, D. Hesse, C. Etz, J. Henk, A. Ernst, I. V. Maznichenko, W. Hergert & I. Mertig. Tailoring magnetic interlayer coupling in $\text{La}_{0.7}\text{Sr}_{0.3}\text{MnO}_3/\text{SrRuO}_3$ superlattices. *Phys. Rev. Lett.* **104**, 167203 (2010).
- [13] M. Verissimo-Alves, P. Garcia-Fernandez, D. I. Bilc, P. Ghosez & J. Junquera. Highly confined spin-polarized two-dimensional electron gas in $\text{SrTiO}_3/\text{SrRuO}_3$ superlattices. *Phys. Rev. Lett.* **108**, 107003 (2012).
- [14] A. J. Grutter, B. J. Kirby, M. T. Gray, C. L. Flint, U. S. Alaan, Y. Suzuki & J. A. Borchers. Electric field control of interfacial ferromagnetism in $\text{CaMnO}_3/\text{CaRuO}_3$ heterostructures. *Phys. Rev. Lett.* **115**, 047601 (2015).

- [15] L. Si, Z. Zhong, J. M. Tomczak & K. Held. Route to room-temperature ferromagnetic ultrathin SrRuO₃ films. *Phys. Rev. B* **92**, 041108(R) (2015).
- [16] H. T. Dang, J. Mravlje, A. Georges & A. J. Millis. Electronic correlations, magnetism, and Hund's rule coupling in the ruthenium perovskites SrRuO₃ and CaRuO₃. *Phys. Rev. B* **91**, 195149 (2015).
- [17] M. Kim & B. I. Min. Nature of itinerant ferromagnetism of SrRuO₃: A DFT+DMFT study. *Phys. Rev. B* **91**, 205116 (2015).
- [18] D. Kan, R. Aso, R. Sato, M. Haruta, H. Kurata & Y. Shimakawa. Tuning magnetic anisotropy by interfacially engineering the oxygen coordination environment in a transition metal oxide. *Nat. Mater.* **15**, 432 (2016).
- [19] V. Granata, L. Capogna, F. Forte, M.-B. Lepetit, R. Fittipaldi, A. Stunault, M. Cuoco & A. Vecchione. Spin-orbital nature of the high-field magnetic state in the Sr₄Ru₃O₁₀. *Phys. Rev. B* **93**, 115128 (2016).
- [20] H. Boschker, T. Harada, T. Asaba, R. Ashoori, A. V. Boris, H. Hilgenkamp, C. R. Hughes, M. E. Holtz, L. Li, D. A. Muller, H. Nair, P. Reith, X. Renshaw Wang, D. G. Schlom, A. Soukiassian & J. Mannhart. Ferromagnetism and Conductivity in Atomically Thin SrRuO₃. *Phys. Rev. X* **9**, 011027 (2019).
- [21] L. Klein, J. S. Dodge, C. H. Ahn, G. J. Snyder, T. H. Geballe, M. R. Beasley & A. Kapitulnik. Anomalous Spin Scattering Effects in the Badly Metallic Itinerant Ferromagnet SrRuO₃. *Phys. Rev. Lett.* **77**, 2774 (1996).
- [22] A. J. Grutter, F. J. Wong, E. Arenholz, A. Vailionis & Y. Suzuki. Evidence of high-spin Ru and universal magnetic anisotropy in SrRuO₃ thin films. *Phys. Rev.*

- B* **85**, 134429 (2012).
- [23] X. K. Ning, Z. J. Wang & Z. D. Zhang. Anisotropy of electrical and magnetic transport properties of epitaxial SrRuO₃ thin films. *J. Appl. Phys.* **117**, 093907 (2015).
- [24] M. Gu, K. Wang, Y. Wang, Q. Xie, H. Cai, G.-P. Zhang & X. Wu. Enhancement of orbital ordering and spin polarization by controlling the dimensionality of the octahedra network. *npj Quantum Materials* **1** (2016).
- [25] J. Matsuno, N. Ogawa, K. Yasuda, F. Kagawa, W. Koshibae, N. Nagaosa, Y. Tokura & M. Kawasaki. Interface-driven topological Hall effect in SrRuO₃-SrIrO₃ bilayer. *Sci. Adv.* **2**, e1600304 (2016).
- [26] L. Wang, Q. Feng, Y. Kim, R. Kim, K. H. Lee, S. D. Pollard, Y. J. Shin, H. Zhou, W. Peng, D. Lee, W. Meng, H. Yang, J. H. Han, M. Kim, Q. Lu & T. W. Noh. Ferroelectrically tunable magnetic skyrmions in ultrathin oxide heterostructures. *Nat. Mater.* **17**, 1087 (2018).
- [27] Y. Ohuchi, J. Matsuno, N. Ogawa, Y. Kozuka, M. Uchida, Y. Tokura & M. Kawasaki. Electric-field control of anomalous and topological Hall effects in oxide bilayer thin films. *Nat. Commun.* **9**, 213 (2018).
- [28] Q. Qin, L. Liu, W. Lin, X. Shu, Q. Xie, Z. Lim, C. Li, S. He, G. M. Chow & J. Chen. Emergence of Topological Hall Effect in a SrRuO₃ Single Layer. *Adv. Mater.* **31**, 1807008 (2019).
- [29] D. Toyota, I. Ohkubo, H. Kumigashira, M. Oshima, T. Ohnishi, M. Lippmaa, M. Takizawa, A. Fujimori, K. Ono, M. Kawasaki & H. Koinuma. Thickness-

- dependent electronic structure of ultrathin SrRuO₃ films studied by in situ photoemission spectroscopy. *Appl. Phys. Lett.* **87**, 162508 (2005).
- [30] S. Kang, Y. Tseng, B. H. Kim, S. Yun, B. Sohn, B. Kim, D. McNally, E. Paris, C. H. Kim, C. Kim, T. W. Noh, S. Ishihara, T. Schmitt & J.-G. Park. Orbital-selective confinement effect of Ru 4*d* orbitals in SrRuO₃ ultrathin film. *Phys. Rev. B* **99**, 045113 (2019).
- [31] H. G. Lee, L. Wang, L. Si, X. He, D. G. Porter, J. R. Kim, E. K. Ko, J. Kim, S. M. Park, B. Kim, A. T. S. Wee, A. Bombardi, Z. Zhong & T. W. Noh. Atomic-Scale Metal-Insulator Transition in SrRuO₃ Ultrathin Films Triggered by Surface Termination Conversion. *Adv. Mater.* **32**, e1905815 (2020).
- [32] J. M. Rondinelli, M. Stengel & N. A. Spaldin. Carrier-mediated magnetoelectricity in complex oxide heterostructures. *Nat. Nanotechnol.* **3**, 46 (2008).
- [33] L. Si, O. Janson, G. Li, Z. Zhong, Z. Liao, G. Koster & K. Held. Quantum Anomalous Hall State in Ferromagnetic SrRuO₃ (111) Bilayers. *Phys. Rev. Lett.* **119**, 026402 (2017).
- [34] W. Shockley. The theory of p-n junctions in semiconductors and p-n junction transistors. *Bell System Technical Journal* **28** (1949).
- [35] E. J. Guo, Y. Liu, C. Sohn, R. D. Desautels, A. Herklotz, Z. Liao, J. Nichols, J. W. Freeland, M. R. Fitzsimmons & H. N. Lee. Oxygen Diode Formed in Nickelate Heterostructures by Chemical Potential Mismatch. *Adv. Mater.* **30**, 1705904 (2018).

- [36] W. Lu, P. Yang, W. D. Song, G. M. Chow & J. S. Chen. Control of oxygen octahedral rotations and physical properties in SrRuO₃ films. *Phys. Rev. B* **88**, 214115 (2013).
- [37] M. E. Fisher & J. S. Langer. Resistive Anomalies at Magnetic Critical Points. *Phys. Rev. Lett.* **20**, 665 (1968).
- [38] M. Ziese, I. Vrejoiu & D. Hesse. Structural symmetry and magnetocrystalline anisotropy of SrRuO₃ films on SrTiO₃. *Phys. Rev. B* **81**, 184418 (2010).
- [39] A. Kanbayasi. Magnetic properties of SrRuO₃ single crystal. *J. Phys. Soc. Jpn.* **41**, 1876 (1976).
- [40] P. B. Allen, H. Berger, O. Chauvet, L. Forro, T. Jarlborg, A. Junod, B. Revaz & G. Santi. Transport properties, thermodynamic properties, and electronic structure of SrRuO₃. *Phys. Rev. B* **53**, 4393 (1996).
- [41] D. J. Singh. Electronic and magnetic properties of the 4*d* itinerant ferromagnet SrRuO₃. *J. Appl. Phys.* **79**, 4818 (1996).
- [42] S. N. Bushmeleva, V. Y. Pomjakushin, E. V. Pomjakushina, D. V. Sheptyakov & A. M. Balagurov. Evidence for the band ferromagnetism in SrRuO₃ from neutron diffraction. *J. Magn. Magn. Mater.* **305**, 491 (2006).
- [43] N. Pavlenko, T. Kopp, E. Y. Tsymbal, J. Mannhart & G. A. Sawatzky. Oxygen vacancies at titanate interfaces: Two-dimensional magnetism and orbital reconstruction. *Phys. Rev. B* **86**, 064431 (2012).
- [44] M. Mlynarczyk, K. Szot, A. Petraru, U. Poppe, U. Breuer, R. Waser & K. Tomala. Surface layer of SrRuO₃ epitaxial thin films under oxidizing and

reducing conditions. *J. Appl. Phys.* **101**, 023701 (2007).

- [45] A. Walsh, C. R. A. Catlow, A. G. H. Smith, A. A. Sokol & S. M. Woodley. Strontium migration assisted by oxygen vacancies in SrTiO₃ from classical and quantum mechanical simulations. *Phys. Rev. B* **83**, 220301(R) (2011).
- [46] T. Leisegang, H. Stocker, A. A. Levin, T. Weissbach, M. Zschornak, E. Gutmann, K. Rickers, S. Gemming & D. C. Meyer. Switching Ti valence in SrTiO₃ by a dc electric field. *Phys. Rev. Lett.* **102**, 087601 (2009).

Main figures:

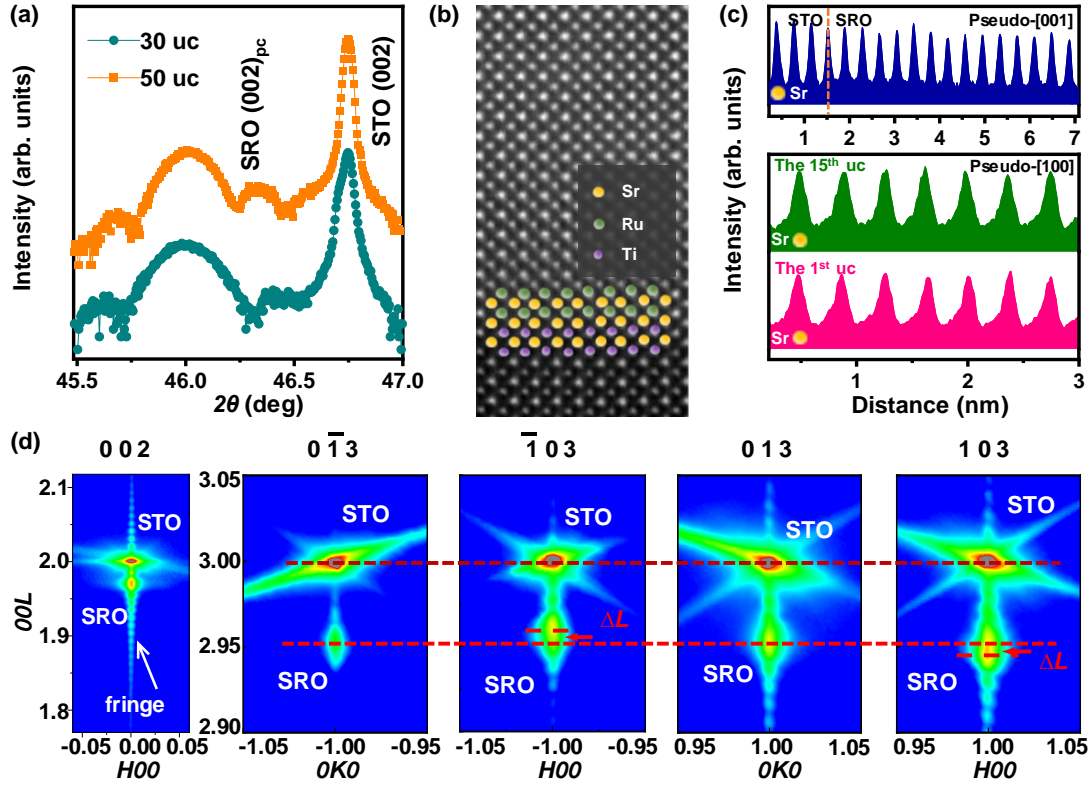


FIG. 1. High-quality Monoclinic SRO thin films without strain relaxation. (a) The θ - 2θ SXRD spectra for (002)-oriented sets of peaks in the 30 uc and 50 uc samples. The SRO thin film is the pseudocubic phase (pc). (b) High-resolution cross-section STEM image of 50 uc SRO thin film. (c) Line profiles of the SrO layers below 15 uc at the pseudo [001] orientation (top panel) and line profiles of the SrO layers for the 1st uc and the 15th uc of the SRO thin film (bottom panel). (d) RSM for 50 uc SRO on STO (001) around (002) and {103} STO Bragg reflection in the reciprocal lattice units of STO with the thickness fringes. The dissimilar values (ΔL) indicate the monoclinic structure, where cell parameters measured for 50 uc SRO thin film are $a_{pc} = 3.905$ Å, $b_{pc} = 3.905$ Å, $c_{pc} = 3.967$ Å, $\alpha = 90^\circ$, $\beta = 89.82^\circ$ and $\gamma = 90^\circ$.

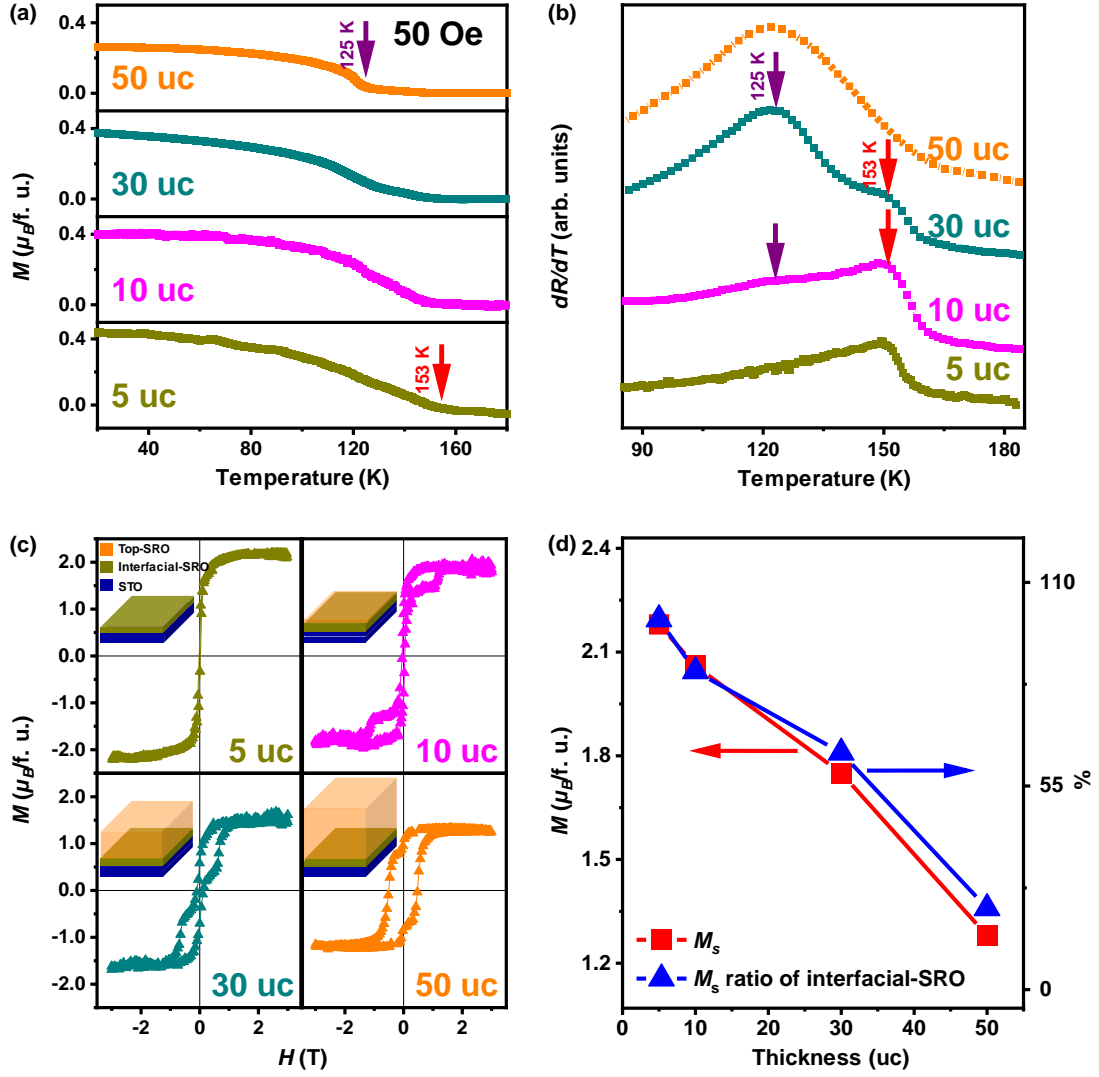


FIG. 2. Emergent interfacial magnetic phase with an enhanced magnetization. (a) Temperature-dependent magnetization (M - T curves) under a magnetic field of 50 Oe. The red and purple arrows indicate the T_C of ~ 153 K and ~ 125 K, respectively. (b) Temperature-dependent differential resistivity (dR/dT - T) shows that the T_C are consistent with the ones from M - T curves, indicating that the interfacial-SRO contributes to the high T_C . (c) Out-of-plane magnetic-field-dependent magnetization (M - H curves) at 10 K. Insets are the schematics of the interfacial-SRO and top-SRO phases. (d) Thickness-dependent out-of-plane M_s (red curves) and its contribution from the interfacial-SRO (blue curves). As the thickness increases, the M_s decreases, which

indicates that the interfacial-SRO contributes to the enhancement of M_s . All the above data obtained from the monoclinic SRO thin films with thicknesses of 5 uc, 10 uc, 30 uc and 50 uc.

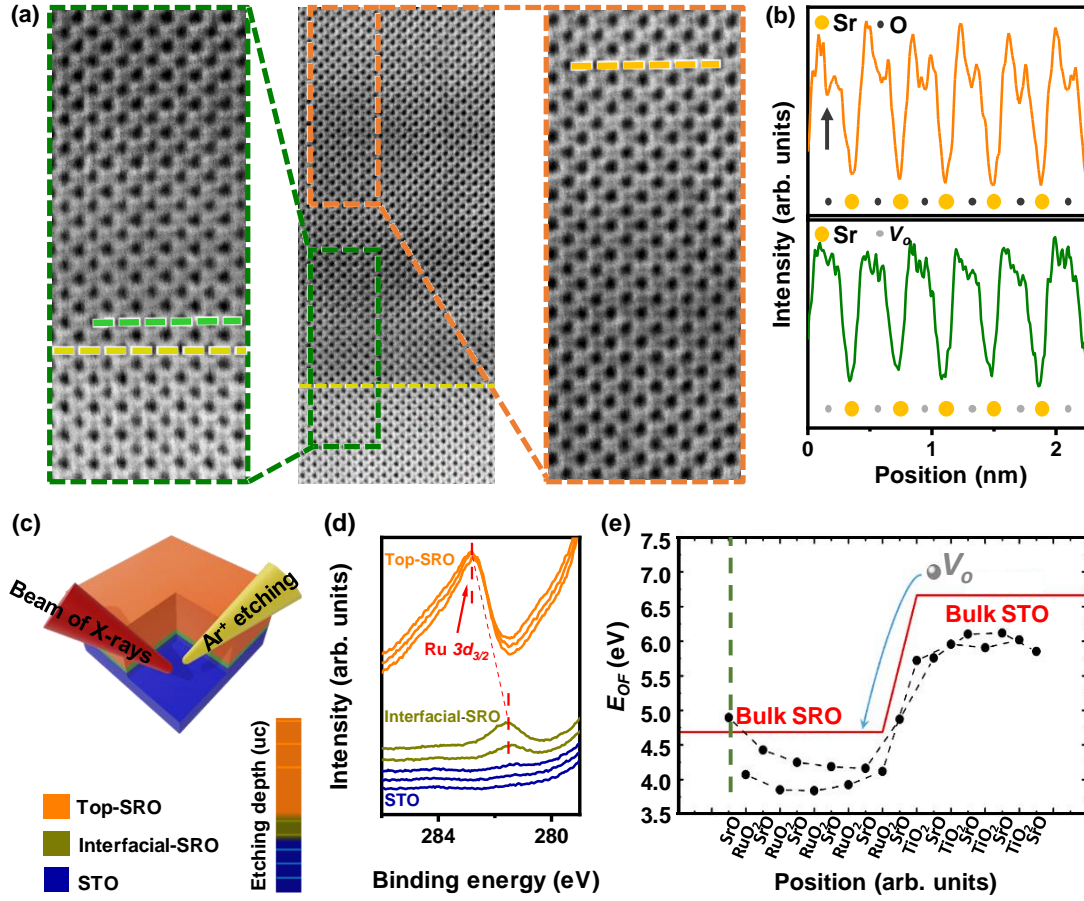


FIG. 3. Evidence of the interfacial-SRO phase driven by an ionic chemical junction. (a) Bright-field STEM of the SRO on STO. The left and right panels show the magnified bright-field STEM image as labeled by the green and orange dashed rectangle box in the middle panel. (b) The corresponding line profile for the detailed atomic structure of SrO layers in the interfacial-SRO (green curve) and top-SRO (orange curve). The yellow, dark grey and light grey dots represent the positions of Sr, O and V_o , respectively. The shallow valleys in the orange curve represent oxygen sites, which are negligible in the green curve, indicating more V_o located at the interface. (c) Schematic of the depth-profile XPS measurements with *in-situ* Ar^+ etching. The orange, yellow and blue zones represent top-SRO, interfacial-SRO and STO, respectively. (d) Depth-profile binding energies of Ru $3d_{3/2}$ shows a dramatic change of binding energies for Ru $3d_{3/2}$. (e)

Calculation of the formation energies and diffusion barriers of V_o across SRO/STO interface. The black dots are the formation energies E_{OF} of the V_o located at different layers across SRO/STO interface. The red lines are the bulk values of SRO and STO at $\sqrt{2} \times \sqrt{2} \times 4$ dimension. The grey sphere indicates the V_o prefers to diffuse from STO into SRO and be prevented at the position of green dash line (diffusion length).

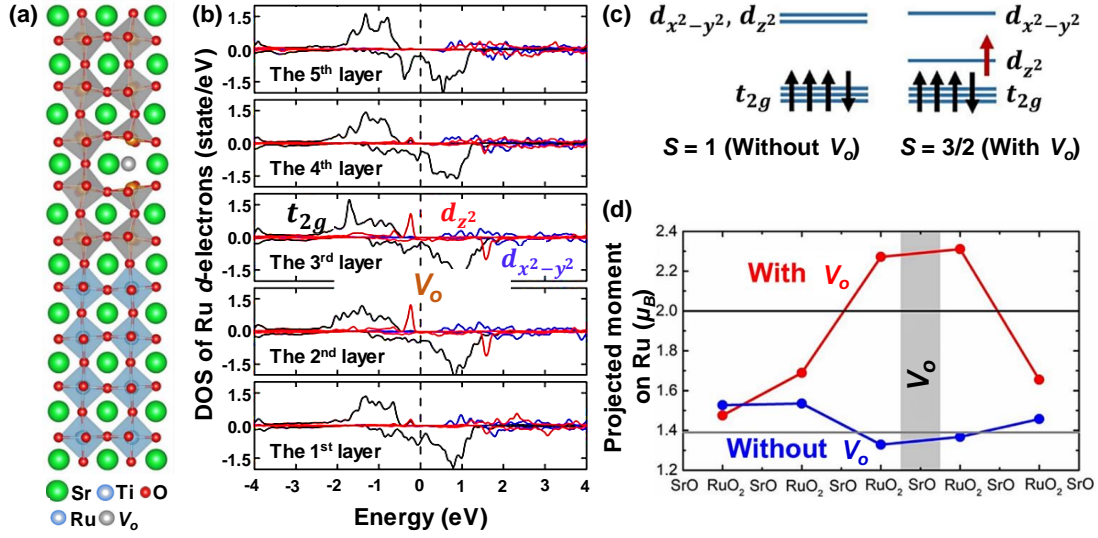


FIG. 4. Microscopic origin of the interfacial high-spin SRO. V_o -induced orbital reconstruction turns initial $4d^4$ low-spin state ($S = 1$) into $4d^5$ high-spin state ($S = 3/2$). In addition, the local magnetic moments of Ru sites neighboring the V_o are significantly larger than that of other Ru sites far away from V_o . Moreover, they are beyond the upper limit of low-spin states predicted by Hund's rule for Ru^{4+} ($t_{2g}^3 \uparrow$, $t_{2g}^1 \downarrow$, $2 \mu_B/\text{Ru}$), which supports the emergence of high-spin state. (a) The crystal structure of SRO/STO heterostructure used in calculations, where four STO substrate layers and five SRO layers are constructed, and an oxygen atom is removed to model V_o . The green, light blue, orange, and red balls represent Sr, Ti, Ru, and O atoms, respectively. The V_o is indicated by grey ball. (b) DFT-resulted layer-dependent DOS of Ru d -electrons. The V_o is set in between the 2nd and 3rd RuO₂ layer. (c) The schematic illustrations of electronic configuration of low-spin state without V_o and high-spin state with V_o . (d) Projected magnetic moments on Ru atoms with (red dots) or without (blue dots) V_o . The V_o locates between the second and third RuO₂ layer as indicated by the grey area. The

black and grey lines are the upper limit of low-spin state and projected moment on Ru atoms in bulk SRO, respectively.

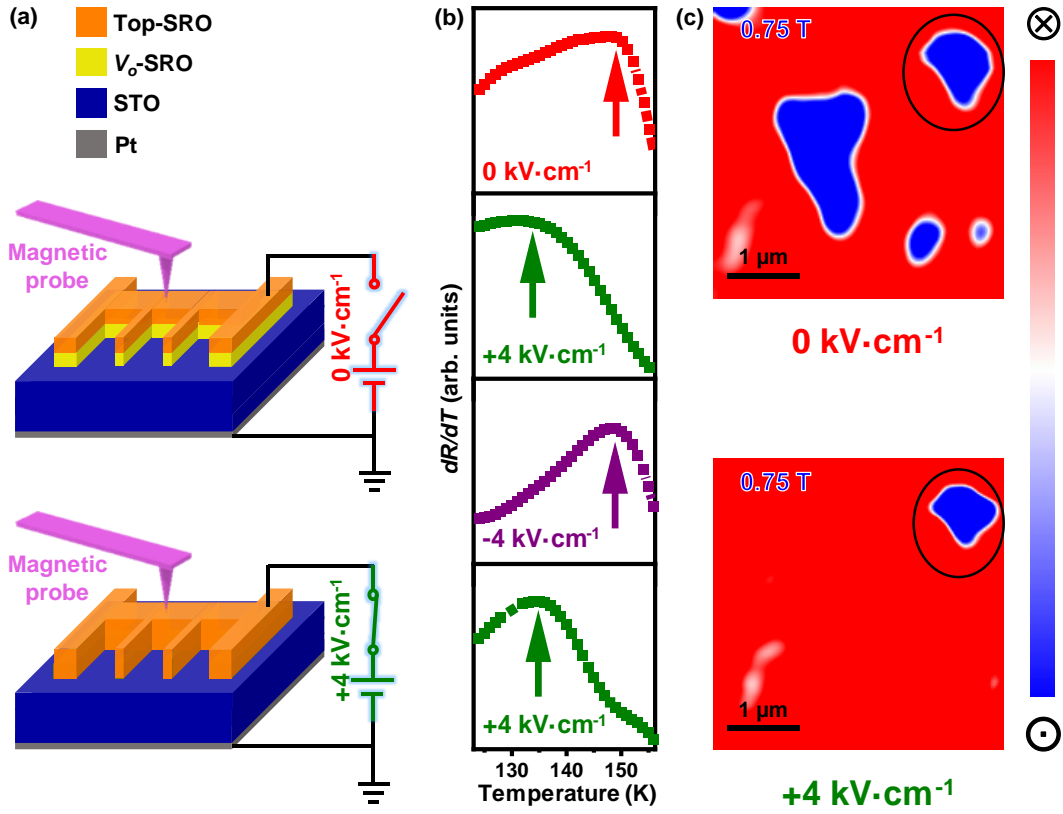


FIG. 5. Electric-field control of T_C and mesoscopic domains switching. (a) Schematics of electrical transport under an electric field with *in-situ* MFM measurement in a solid-state ionic gating device. (b) Reversible control of T_C derived from dR/dT - T curves (the red, green and purple arrows) due to the erasing and rebuilding of the V_o -SRO with the application of the vertical electric field of 0, +4, -4, +4 kV·cm⁻¹. (c) Magnetic domain switching in top-SRO/ V_o -SRO (total thickness of 10 uc) without/with the application of electric field, where the magnetic domains were captured at 0.75 T and 10 K with/without V_o -SRO. The black circles indicate that the images were captured at the same area. The scale bar is 1 μm.